Aerodynamic performance and flow evolution of a high-speed train exiting a tunnel with crosswinds

Lei Wang [a,b], Jianjun Luo [a,b,*], Feilong Li [a,b], Dilong Guo [c,d], Liping Gao [a,b], Dengke Wang [a,b]

[a] Key Laboratory of Urban Underground Engineering of the Ministry of Education, Beijing Jiaotong University, Beijing, 100044, China
[b] Beijing's Key Laboratory of Structural Wind Engineering and Urban Wind Environment, Beijing Jiaotong University, Beijing, 100044, China
[c] Key Laboratory of Mechanics in Fluid Solid Coupling System, Institute of Mechanics, Chinese Academy of Sciences, Beijing, 100190, China
[d] Institute of Mechanics, Chinese Academy of Sciences, Beijing, 100190, China

ABSTRACT

Sudden changes in the aerodynamic loads acting on trains can result in derailment or overturning. The impacts of infrastructure scenarios on the aerodynamic performance of trains are significant. When high-speed trains travel from one infrastructure scenario to another one, the aerodynamic loads and flow field will change suddenly. It is a commonly in western China for HSTs to exit a tunnel with crosswinds. In order to investigate the aerodynamic loads and the flow evolution, a three-dimensional, compressible, unsteady Reynolds Averaged Navier-Stokes method was utilized to simulate the process of a train exiting a tunnel under crosswinds. Results show that the flow field and the pressure varied significantly in the horizonal plane while the train exited the tunnel under crosswinds. In addition, the aerodynamic loads of each carriage which varied abruptly resulted in complex dynamic responses of the train including lateral variation, snake-like locomotion, and pitching motion. Furthermore, the variation magnitudes of ΔC_{side}, ΔC_{lift}, and ΔC_{RM} for the head carriage were 4.1, 2.2 and 1.6 times for the middle carriage, and 7.9, 8.1 and 8.2 times for the rear carriage. Therefore, the aerodynamic performance of the head carriage was the worst and the risk of accidents was the highest under crosswinds.

1. Introduction

By the end of 2020, the operating range of China's high-speed railway system reached 38,000 km. Currently, China is rapidly constructing a high-speed railway network in western regions, and the Sichuan-Tibet high-speed railway is one of the most important railway lines, with a total length of 1742.4 km, including 1011 km of newly built line from Ya'an to Nyingchi. The total length of bridges and tunnels is 965.74 km. More than 70 tunnels with a total length of 851.48 km will be built, accounting for 74.43% of the total length of the line. Therefore, connections between tunnels and flat ground, as well as tunnels and bridges, will be more common during operation. In addition, wind-sand disasters are severe in China's western regions. The Baili wind area is one of the four most famous wind areas in China, and the maximum wind speed can exceed 60 m/s (Sun et al., 2019a).

With developments of the lighter and faster modern railway trains (Suzuki, 2016), crosswinds have emerged as one of the most important factors affecting train safety (Cooper, 1980; Baker, 2009; Zhuang and Lu, 2015). When train speed exceeds 200 km/h and the crosswind speed is greater than 30 m/s, the train is most likely to derail or overturn (Hoppmann et al., 2002; Fujii et al., 1999). Recently, train accidents induced by crosswinds have occurred in many countries worldwide including New Zealand, the UK, Japan, and China (Sun et al., 2019; Hosoi, 2011; Baker, 2010; Hemida, 2010; Suzuki et al., 2003; Cooper, 1981).

In recent decades, the influence of crosswinds on high-speed train has received extensive attention (Tomasini et al., 2014; Xiang et al., 2018), including the study of the influences of crosswinds on the aerodynamic performance of HSTs passing through different infrastructure scenarios, such as on flat ground (Guo et al., 2019; Rocchi et al., 2018; Niu et al., 2017), embankments (Baker, 1985; Guo et al., 2020; Tomasini et al., 2014; Diedrichs et al., 2007), cuttings (Zhang et al., 2015; Liu et al., 2018), bridges (Montenegro et al., 2020; Yao et al., 2020; He et al., 2014), and wind barriers (Xue et al., 2020; He et al., 2014). In particular, Chen et al. (2020) and Wang et al. (2020) analyzed the influence of various infrastructure scenarios on HSTs under crosswinds using CFD

simulations. They concluded that the aerodynamic characteristics of trains exist significant distinction when the trains running in different infrastructure scenarios.

Researchers have mainly concentrated on the impact of crosswinds on the aerodynamic characteristics of trains running in a single infrastructure scenario. When high-speed trains move from one infrastructure scenario to another under crosswinds, the pressure field and the flow field vary rapidly. The aerodynamic loads acting on the train change accordingly, which is a critical factor of train accidents. For example, trains on the Lan-Xin line (Lanzhou-Xinjiang) are prone to overturning in the "Baili wind area" in China. In 2007, the first five carriages of the No. 5807 passenger train overturned at the end of a wind barrier (Tian, 2010). This was due to the sudden increase in the aerodynamic loads when leaving the wind barrier under high-speed crosswinds, which led to significant deterioration of the aerodynamic performance and train overturning. Therefore, it is necessary to investigate the aerodynamic behaviors of a train traveling from one infrastructure scenario to a different one.

When a train leaves a tunnel with a crosswind, the horizontal swing induced by the aerodynamic lateral load significantly affects the train operation safety and passenger comfort. Therefore, it is extremely important to investigate the aerodynamic performance of a train exiting a tunnel under strong crosswinds. However, few studies on the aerodynamic performance of trains exiting a tunnel under crosswind conditions have been reported.

At present, methods for studying the influence of crosswind effects mainly include full-scale tests, model experiments, and computational fluid dynamics (CFD) simulations. Full-scale tests can measure the aerodynamic parameters directly and effectively in a real environment (Zhang et al., 2015). Suzuki (2016) studied the aerodynamic characteristics of a full-scale train under crosswinds, and they concluded that the critical wind speed for the train overturning was related to the incident angle of the crosswind as well as the train speed. Baker (2004) measured the unsteady aerodynamic forces and moments acting on a train on flat ground using a full-scale train. Owing to the long duration and the difficulty of controlling the experimental conditions (Gallagher et al., 2018; Dorigatti et al., 2015; Khier et al., 2000), this method is rarely used.

Compared with full-scale tests, model tests have the advantages of low cost and easy operation. Model tests can be subdivided into wind tunnel tests and dynamic model tests according to the motion state of the train. Wind tunnel tests are the most widely utilized, but they cannot reflect the relative movement of the train. Dynamic model tests followed the wind tunnel tests later (Baker, 1986); these tests can reproduce the relative movement between the train and the ground. The situation in which a train passes through a tunnel and when two trains pass each other in a tunnel can be carried out using dynamic model tests (Yang et al., 2013, 2016). Wang et al. (2020), Bocciolone et al. (2008), Li et al. (2018), Cheli et al. (2010), and Schober et al. (2010) concluded that the differences between the dynamic and static model test were related to the train operating environment.

In recent years, with the development of computer technology, CFD simulation has been extensively used. Sun et al. (2019a, b) studied the aerodynamic characteristics of a high-speed train passing through a breach between two windbreaks under strong crosswinds. Chen et al. (2017) and Zhou et al. (2017) investigated the influence of ambient wind on the pressure wave in a tunnel when a single train passed through a tunnel and two trains meeting in a tunnel. However, the pressure wave in the tunnel was analyzed only and they did not consider the impact of ambient wind on the aerodynamic performance of the train. Deng et al. (2019) numerically investigated the aerodynamic loads and traffic safety of two windproof facilities, including windbreak (WB) and an anti-wind open-cut tunnel (AOT), when a HST passed through them under crosswind conditions. The results showed that the AOT is more effective than the WB in terms of windproof effects. Yang et al. (2020) focused on the aerodynamic behaviors and operational stability

of a HST entering a tunnel in a crosswind environment. The research was useful for assessing the operational safety of a running HST subjected crosswind. Miao et al. (2020) numerically investigated the aerodynamic performance of a high-speed train passing through tunnel junctions under crosswind. Overall, existing research mainly focused on conditions including low train speed or low crosswind speed, and thus may not reflect actual situations.

In this study, three-dimensional compressible, viscous, unsteady Reynolds-averaged Navier-Stokes (URANS) simulations were performed to establish a numerical model including crosswind, tunnel and a train. The motion of the train relative to the tunnel was realized by the sliding mesh method. This study focused on the characteristics of the aerodynamic loads and the flow field evolution of the train during the process of the train exiting a tunnel into crosswind conditions to reveal the interaction mechanism between the crosswind, train, and tunnel. The results provide a more comprehensive understanding and reference for train operation safety as a high-speed train exits a tunnel to open air under crosswinds.

2. Methodology

2.1. Governing equations

A three-dimensional, compressible, and unsteady flow field is generated when a HST moves at high speed (Li et al., 2019; Yang et al., 2018). It is very important to select a reasonable turbulence model for the calculation, which directly determines the reliability of the simulation. The Reynolds Averaged Navier-Stokes (RANS) equations describe the time-averaged flow, and it is currently the most widely used method (Liu et al., 2018). The shear-stress transport (SST) $k - \omega$ turbulence model has various advantages, including a high calculation accuracy and low calculation cost. In particular, the accuracy and stability of the SST $k - \omega$ model is much better than other models, and it can accurately capture the characteristics of separation flow (Catalano et al., 2003; Menter et al., 2003). Li et al. (2019) investigated the influence of six turbulence models on aerodynamic behaviors of high-speed train under crosswinds. By comparing the numerical simulations with the experimental results, the results show that the SST $\kappa - \omega$ model is most suitable for the numerical simulation of the aerodynamic behavior of trains in crosswinds.

Therefore, a three-dimensional, compressible, unsteady RANS equation and SST $k - \omega$ turbulence model were selected for this study. This model has been extensively used to study the influence of crosswinds on the aerodynamic performances of trains (Yao et al., 2020; Li et al., 2019; Liu et al., 2018; Horvat et al., 2020).

The SST $k - \omega$ turbulence model can be expressed as follows:

$$\frac{\partial \rho \kappa}{\partial t} + \frac{\partial}{\partial x_i}\left[\rho u_i \kappa - (\mu + \sigma_\kappa \mu_t)\frac{\partial \kappa}{\partial x_j}\right] = \tau_{tij}S_{ij} - \beta^* \rho \omega \kappa \tag{1}$$

$$\frac{\partial \rho \omega}{\partial t} + \frac{\partial}{\partial x_i}\left[\rho u_i \omega - (\mu + \sigma_\omega \mu_t)\frac{\partial \omega}{\partial x_j}\right] = P_\omega - \beta \rho \omega^2 + 2(1 - F_1)\frac{\rho \sigma_{\omega 2}}{\omega}\frac{\partial \kappa \partial \omega}{\partial x_i \partial x_j} \tag{2}$$

where t is time; ρ is the density of the air; κ refers to the turbulence kinetic energy; ω is the turbulence dissipation ratio; x_j refers to the position, where the subscripts $j = 1$, 2, and 3 represent the x-, y-, and z-directions, respectively; u_j refers to the components of the slipstream; σ_ω, $\sigma_{\omega 2}$, σ_κ, β, β^*, and γ are empirical constants; F_1 refers to a switch function, and μ_t is the vortex viscosity coefficient.

2.2. Computational model

The high-speed train model is presented in Fig. 1. The train prototype was a CRH380A high-speed EMU, which is widely used in China's high-speed railways. The width and height of the train were W = 3.38 m
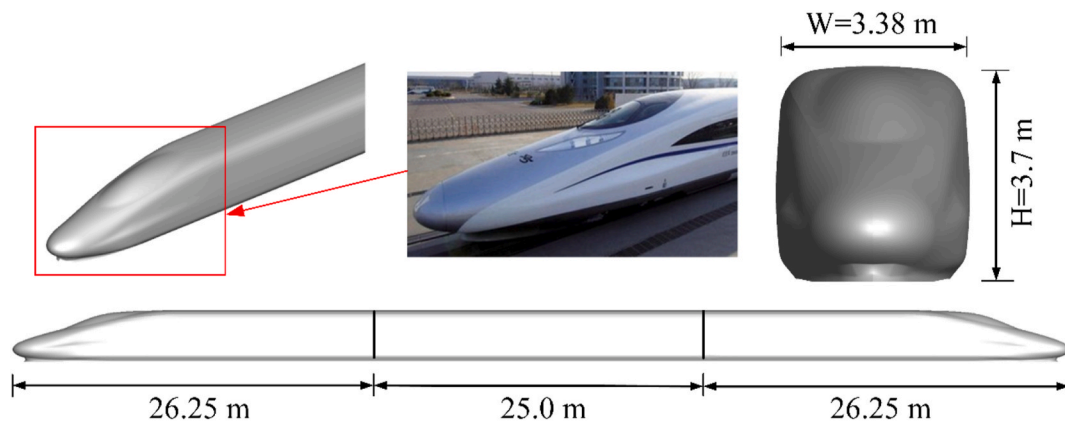
Fig. 1. Full-scale three-carriage train model.

and H = 3.70 m, respectively. The cross-sectional area was 11.2 m². As the shape of the cross section on the middle carriages remained unchanged, the flow structure in the boundary layer tended to be stable when air flowed a certain distance from the nose tip of the head carriage, and the aerodynamic forces changed slightly (Suzuki et al., 2003; Khier et al., 2000; Ford, 2003). Therefore, a full-scale, three-carriage train model was adopted, and the shapes of the head and rear vehicles were the same. The total length of the train was L = 77 m. Other structural details, such as the pantograph, the bogie, and the door handles, were ignored.

The tunnel model was the double-track tunnel suitable for 350 km/h HSTs in China. The width and height were 13.2 m and 8.78 m, respectively. The clearance area was 100 m², and the centerline distance between two tracks was 5.0 m, as shown in Fig. 2. To reduce the calculation cost, the tunnel was 500 m in length. The distance between the bottom of the train and the rail top was 0.2 m. The train ran at the speed of 350 km/h (97.22 m/s), and the corresponding Reynolds number $Re = 2.46 \times 10^7$ when the characteristic length was selected as the train height H.

The calculation domain of the model is presented in Fig. 3. The distance between the nose tip of the head carriage and the tunnel exit was 145.83 m. According to Clause 5.3.3.4 of BS EN14067-6(2018), the distance from the side of the train to the upstream and downstream boundary surfaces should not be less than 8H and 16H, respectively. Therefore, the dimensions of the exit side domain were length × width × height = 81.1H × 43.2H × 21.6H, and the blocking ratio was about 1.2%. The distances from the windward and leeward side of the train to the corresponding boundary surface were 10.8H and 32.4H,

respectively, which met the requirements of BS EN14067-6(2018). To reduce the mesh resolution, the dimensions of the entrance domain were length × width × height = 27H × 27H × 21.6H.

2.3. Boundary conditions

The boundary conditions of the model are shown in Fig. 4. The surface ABCD was a velocity-inlet boundary with uniform inlet wind speed of 30 m/s. The train surface, tunnel wall, ground surfaces (ADHE, A'D'H'E'), and surfaces adjacent to the tunnel portal (CDGH, A'B'F'E') were no-slip walls. A pressure-outlet condition was applied for the other boundary surfaces, and the pressure value was set at 101,325 Pa.

To reflect the train movement, the dynamic mesh method (DMM) and the sliding mesh method (SMM) are often used in simulations. The DMM is required to regenerate the grid after each iteration, which requires a high mesh quality and higher computational cost. To reduce the computational cost and improve the computational efficiency, the SMM was adopted to simulate the HST movement. Existing studies have shown that the SMM can accurately simulate the relative motion between a train and a tunnel (He et al., 2018; Chu et al., 2014; Xiang et al., 2010; Khayrullina et al., 2015). The moving region contained the train and its surrounding zones, while the other regions were stationary. The information between the two regions was exchanged through the interface after each iteration, as shown in Fig. 5.

2.4. Computational mesh

The computational model was discretized with a structural hexahedral mesh. The areas around the train were the zones of interest. The density of the mesh near the train surface was larger, while the density of the mesh in the area far from the train surface was small. To accurately capture the flow structure in the boundary layer of the train surface, it is very important to determine the thickness of the first layer mesh. According to the ANSYS Fluent help document, SST $\kappa - \omega$ turbulence model is one of the low Reynolds number models, and the $y+$ required by this model is not larger than 1 for the simulations with high accuracy demands on the wall boundary layer. The height of the first mesh in the boundary layer was 1×10^{-5} m, and the corresponding $y+$ was roughly 1. The gradient of the mesh was 1.1, and 12 layers were arranged in the boundary layer, as shown in Fig. 6. The mesh on the head and rear carriage was denser, and the grid element sizes of the middle vehicles were larger, with sizes between 0.1 and 0.5 m. The longitudinal grid length along the tunnel was 0.5 m. The number of structural units was 12.62 million.

2.5. Solution processes

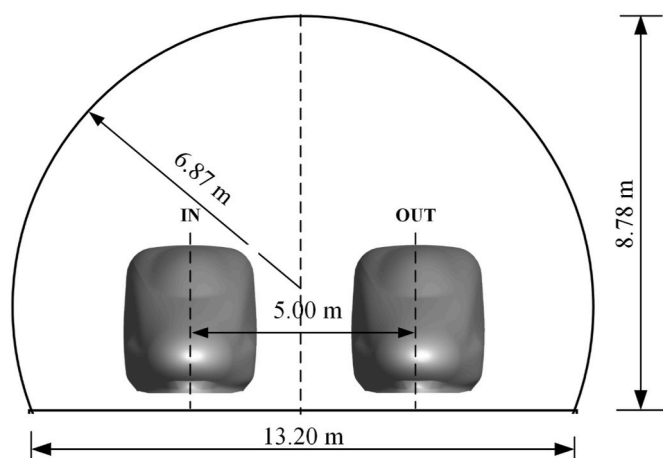The calculations were carried out using ANSYS-FLUENT 17.1

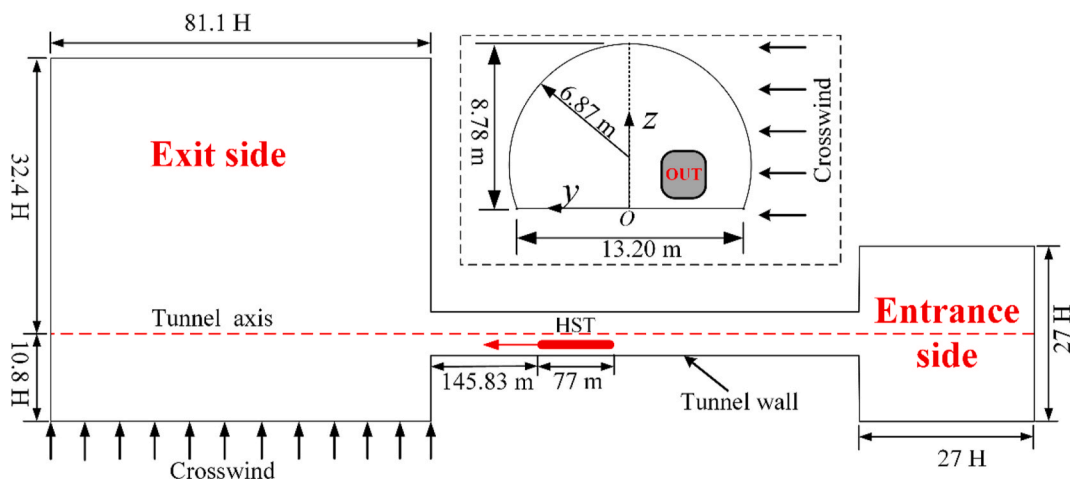**Fig. 2.** Cross section of high-speed railway tunnel in China.

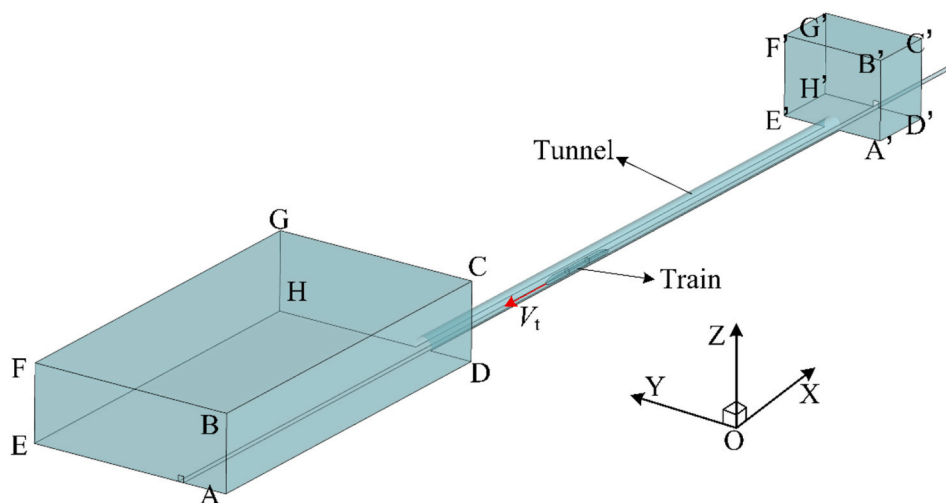**Fig. 3.** Diagram of computational domains.

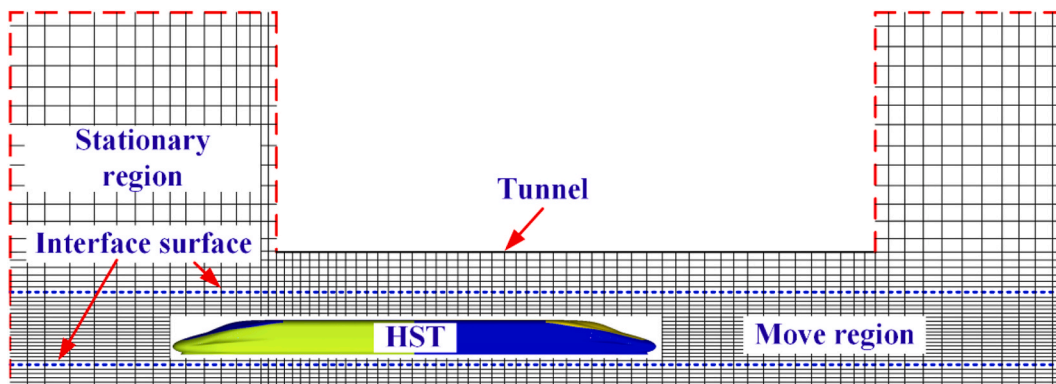**Fig. 4.** Diagram of boundary conditions.

Fig. 5. Diagram of the sliding mesh method.

software. The three-dimensional compressible unsteady Navier-Stokes equations were discretized using the finite volume method (FVM). The SIMPLE (Semi-Implicit Method for Pressure-Linked Equations) algorithm was used for the pressure-velocity coupling (Ferziger and Peric, 2002). The second-order upwind scheme was used to discretize the convection and diffusion terms. The time derivative was discretized by a first-order implicit method. The physical time step size was 1×10^{-3} s,

which less than previously used values of 2.5×10^{-3} s (Yang et al., 2018), 7×10^{-3} s (Baron et al., 2001), and 1.8×10^{-2} s (Chu et al., 2014). Therefore, the step time chosen here was appropriate. The number of iterations at each step was 20, and the residual of the turbulent items were allowed not exceed 10^{-3} for each time step.
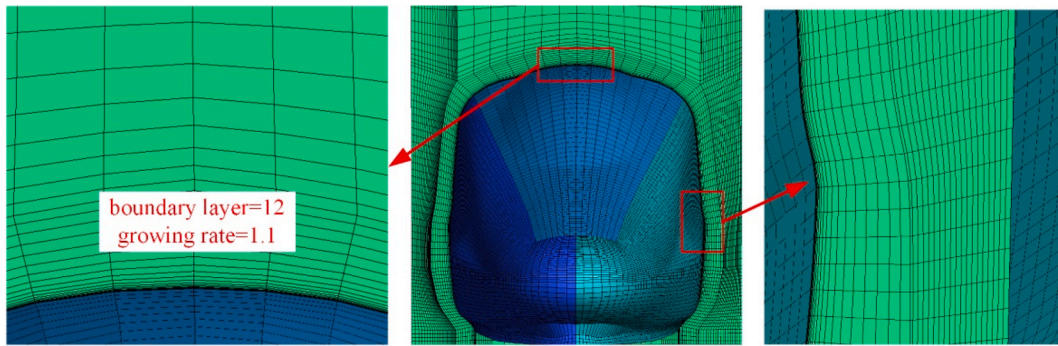
Fig. 6. Boundary layer mesh on train surface.

2.6. Data post-processing

The aerodynamic forces included six aerodynamic physical quantities (lateral force, lift, drag, overturning moment, yawing moment, and pitching moment) that acted on the train under crosswinds. The side force, lift force, and overturning moment are the parameters that affect train safety most significantly under crosswinds. They are defined as follows:

$$Cp = 2(P - P_\infty) / \rho u_w{}^2 \tag{3}$$

$$F_{side} = \frac{1}{2}\rho u_w{}^2 C_{side} A \tag{4}$$

$$F_{lift} = \frac{1}{2}\rho u_w{}^2 C_{lift} A \tag{5}$$

$$M_{RM} = \frac{1}{2}\rho u_w{}^2 C_{RM} A h \tag{6}$$

where C_p, C_{side}, C_{lift}, and C_{RM} are the pressure coefficient, side force coefficient, lift force coefficient, and overturning moment coefficient, respectively; F_{side}, F_{lift}, and M_{RM} are the aerodynamic side force, the lift force, and the overturning moment, respectively; P is the static pressure on the train surface; P_∞ is the static pressure at infinity; ρ is the air density; u_w is the crosswind speed; A and h are the windward area and the height of the train, respectively.

3. Validation

3.1. Verification of mesh independence

To better verify the mesh independence, three calculational models were performed with different grid resolutions: coarse mesh with 1.12×10^7 elements, medium mesh with 1.26×10^7 elements, and fine mesh containing 1.44×10^7 element cells. They contained different numbers of elements in the boundary layer of the train surface. The first grid thickness near the train surface was 1×10^{-5} m, and the boundary layers were arranged with 8, 12, or 18 layers. The HST exited the tunnel into open air under crosswind conditions. The speeds of train and the crosswind were 350 km/h (97.22 m/s) and 30 m/s, respectively.

The curves of maximum C_{side} and C_{lift} with different mesh resolutions of the boundary layer are presented in Fig. 7. C_{side} and C_{lift} decreased with the increase in the number of boundary layer elements. When the number of layers in the boundary layer was 12, the maximum C_{side} and C_{lift} had a tendency to remain stable. Therefore, the mesh with 12 layers in the boundary layer was selected.

3.2. Moving model test validation

To demonstrate the accuracy of the turbulence model, the simulation results were compared with the moving model test (MMT). The MMT was performed at the Advance Railway Mechanics Center (ARMC), Institute of Mechanics, Chinese Academy of Sciences in the Huairou District of Beijing City. The detailed information about the MMT was described by Yang et al. (2013) and Yang et al. (2016). A three-vehicle model was adopted. The train was 9.9 m long, and scale ratio was 1:8. The moving speed was 304 km/h. The tunnel model corresponded to the
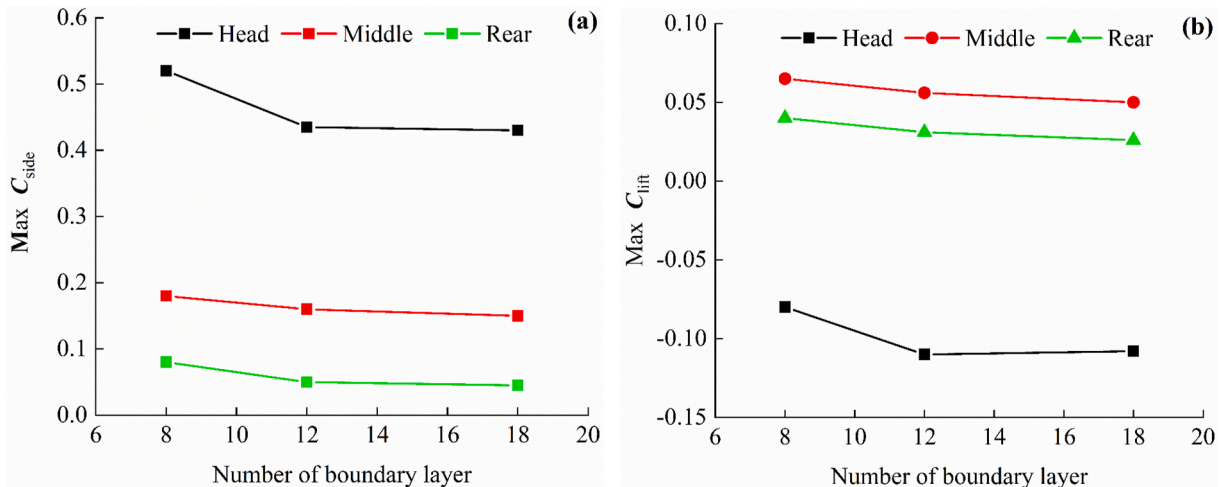

Fig. 7. (a) Max C_{side} and (b) C_{lift} with different boundary layer grids.

double-track tunnels commonly used in China, as shown in Fig. 2. The length of the tunnel was 60 m. The moving model rig was as shown in Fig. 8. The pressure sensor was installed 20 m from the tunnel entrance and 471 mm above the bottom surface. To avoid the dynamic similarity effect, the numerical model was consistent with the MMT.

The comparison of the static pressure from the simulations and experiments is shown in Fig. 9. The numerical and experimental results as the train traveled through the tunnel showed reasonable agreement. The maximum and minimum initial compression wave were 1364 and -2166 Pa in the MMT, respectively, and the variation amplitude was 3530 Pa. The maximum and minimum values of the initial compression wave were 1285 and -2099 Pa in the simulation, respectively, and the variation amplitude was 3384 Pa. The differences in the maximum and minimum initial compression wave and the variation amplitude between the simulation and MMT were 6.1%, 3.2% and 4.3%, respectively. The differences were attributed to the simplifications in the CFD geometry.

Fig. 10 compares the three-dimensional flow field around the train under crosswinds in the present paper with the simulation results of Yang et al. (2018) (Fig. 10(b)) and the wind tunnel test of Copley (1987) (Fig. 10(c)). The dominant flow vortex structures occurred on the leeward side of the head train with a large deflection, which was discovered by Copley (1987). The simulated flow pattern showed strong agreement with the results of Yang et al. (2018) and Copley (1987). The comparisons above verified that the turbulent model adopted in this paper could reliably predict the flow around a train under crosswinds.

4. Results and discussion

4.1. Flow structure

Owing to the piston effect, the air in front of a train is squeezed and flows along the direction of the train movement when the HST moves in a tunnel. The flow direction of the air between the tunnel and the train is opposite to the direction of the train motion. The flow field around the train changes when the train exits the tunnel into crosswind conditions. Fig. 11 displays the flow evolution around the train when the train exited a tunnel into non-crosswind and crosswind conditions.

The flow field distributions in the annular space between the train and tunnel were basically the same, and the slipstream flowed from the head to the rear of the train under different wind conditions, as shown in Fig. 11 (a1) and (a2). The flow field distributions in front of the head carriage were different. Under non-crosswind conditions, the air in front of the train flowed out of the tunnel and diffused around it, and the flow field around the train was always symmetric as the train exited the tunnel, as shown in Fig. 11 (a1)–(g1). In contrast, part of the airflow in front of the head carriage was biased toward the leeward side, and another part of the air flowed into the tunnel again while the train exited the tunnel under crosswind conditions, as shown in Fig. 11 (a2).
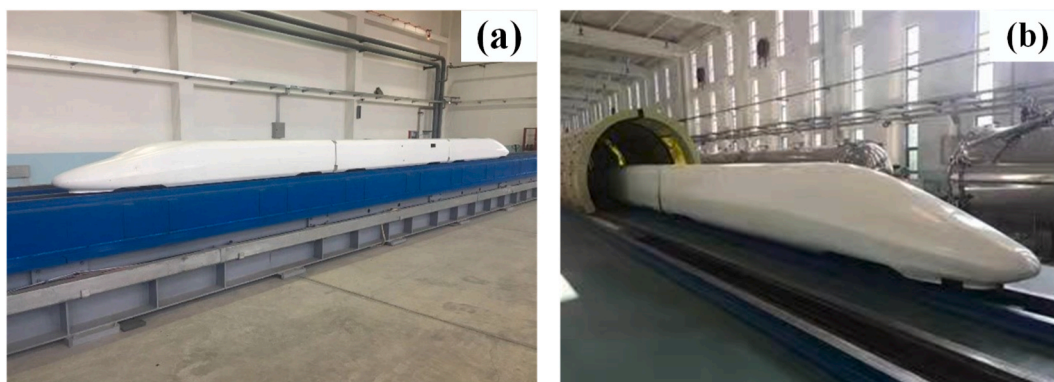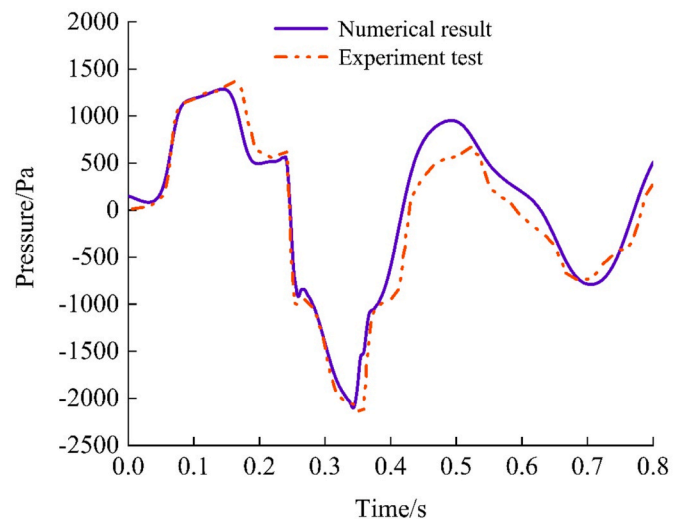

Fig. 9. Comparison of numerical results and experimental test.

As the train exited the tunnel, the impact of the crosswind on the flow field gradually appeared. When the streamline section of the head vehicle exited the tunnel, flow separation occurred on the leeward side, resulting in a local strong negative pressure area, as shown in Fig. 11 (b2) and (c2). As the train continued to exit, the flow separation on the leeward side of the vehicle outside the tunnel fully developed, forming a horizontal vortex structure that deviated from the train leeward side along the train. In addition, a complex flow field appeared behind the tail vehicle in the tunnel, as shown in Fig. 11 (d2) and (f2). Fig. 11 (g2) shows that the vortex on the train leeward side continued to extend to the rear of the train, with a length of about 1L (where L represents the total train length), after the train exited the tunnel completely. Fig. 11 (d2)–(g2) show that the flow field was highly asymmetric, shifting to the train leeward side, when crosswinds existed at the tunnel exit.

The three-dimensional flow field distribution when the train middle arrived at the tunnel exit is illustrated in Fig. 12. The red dotted and solid lines represent the evolution of the flow at the tunnel exit and the vortex structures on the train leeward side, respectively. When the crosswind (shown as A) reached the train windward side, the airflow divided into two parts. A small part of the air (shown as A1) flowed into the tunnel through the gap between the train windward side and the tunnel, and a large portion of the air (shown as A2) bypassed the train and moved downstream. Due to the blocking effect of the tunnel, the airflow (shown as A2) at the tunnel exit was divided into two parts again. Most of the air (shown as A21) flowed into the tunnel, and the rest (shown as A22) moved downstream.

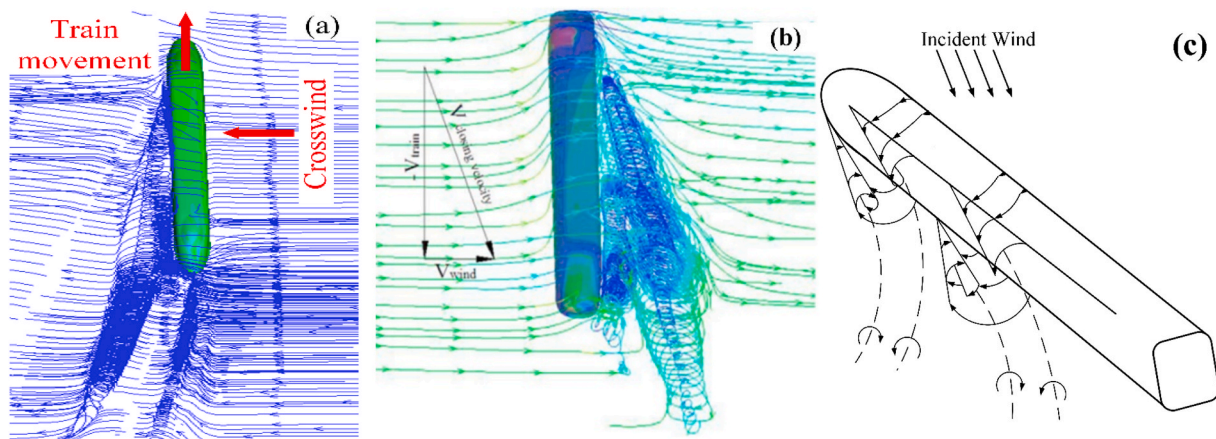A longitudinal vortex system (shown as B) was generated on the train

Fig. 8. Moving model rig of HST.

Fig. 10. Comparison of flow structures in (a) this paper and (b) simulation by Yang et al. (2018) and (c) experiment by Copley (1987).

leeward side, and the size increased along the train under crosswind conditions. The evolution of the vortex changed near the tunnel exit. A portion of the air (shown as B1) suddenly changed its flow direction and entered the tunnel, and the vortices gradually dissipated in the tunnel. The other part of the air (shown as B2) flowed downstream in the direction of the crosswind. Therefore, under crosswind conditions, the interactions between the crosswind, train, and tunnel resulted in a complex flow field at the tunnel exit, which affected the aerodynamic loads acting on the train.

The interactions between the train and tunnel disappeared gradually after the train exited the tunnel completely. The three-dimensional flow distribution as the tail nose was 50 m from the tunnel exit under crosswind conditions was shown in Fig. 13. Five vortex systems, $V1$–$V5$, were evident around the train. $V1$ originated from the end of the streamline section of the head vehicle and developed along the train length. The deviation angle and extension distance of $V1$ were the largest. $V2$ was generated by the flow separation at the train bottom, which only existed in the zone within the train length. Its deviation degree was smaller than that of $V1$. $V3$ was generated on the train windward side, and the size and deviation angle were small. $V4$ was produced by the airflow flowing through the bottom of the tail vehicle, which was similar to $V2$. Compared with $V1$ and $V2$, the dimensions and deviation angles of $V3$ and $V4$ were smaller. In addition to $V1$–$V4$, $V5$ was generated at the tail carriage nose, and the deflection direction was consistent with $V1$.

A simplified flow field is illustrated in Fig. 14(a), corresponding to Fig. 13. $V1$, $V3$, and $V5$ rotated counterclockwise, while $V2$ and $V4$ rotated clockwise. The flow field varied with space, while the HST moved at high speed under crosswind conditions. Hemida et al. (2005) and Hemida and Krajnovi (2010) reviewed the characteristics of the flow field on the leeward side of a stationary train under crosswinds using CFD. The results showed that the flow structures on the leeward side remained stable when the distance from the head carriage nose was larger than 3.5D (D represents the train width). Fig. 14(b) shows the flow fields of a stationary vehicle under different yaw angles obtained by Chiu and Squire (1992). By comparing Fig. 14(a) and (b), it was concluded that the wind tunnel test of the stationary train cannot truly reflect the flow characteristics of a full-scale train. Therefore, it is necessary to consider the movement of the train relative to the surroundings.

4.2. Pressure distribution on train surfaces

The flow field variations around the train inevitably led to a pressure difference on the train surface. Fig. 15 shows the pressure contours on the train surface at the same time as that in Fig. 11. The left and right figures correspond to non-crosswind and crosswind conditions,

respectively.

In the absence of wind, the pressure distributions on both sides of the train were basically symmetric whether the train exited the tunnel or not. Furthermore, there was little difference in the pressure distributions of the train surface inside and outside the tunnel, as shown in Fig. 15 (a1)–(g1). As the train was running in the tunnel, the pressures on the areas around the head vehicle and tail vehicle nose were positive, and the pressure on the middle vehicle was negative, while crosswinds existed at the tunnel exit, as shown in Fig. 15(a2). As shown in Fig. 15 (b2), the position of maximum C_p was biased toward the upstream direction, and the pressure difference on both train sides appeared gradually when the head nose tip reached the tunnel exit. The pressure on the train windward side outside the tunnel was positive, while the pressure on the train leeward side was negative, as shown in Fig. 15(c2)–(e2). The pressure difference on both train sides resulted in a robust aerodynamic side force. In addition, the difference in the aerodynamic loads acting on the train inside and outside the tunnel led to large shear and torsional deformation, which significantly affected the train operating safety. A wake vortex generated behind the HST resulted in an unstable pressure field, as indicated in Fig. 15(f2)–(g2).

The pressure on the train surface varied when the train arrived at the tunnel exit under crosswind conditions. Fig. 16 shows the C_p curves on the train windward and leeward sides of the horizontal cross section 1.50 m above the rail surface as the train middle exited the tunnel. The curves of C_p on the windward are presented in Fig. 16(a). The positive C_p of the nose tip was the largest, with a value of 0.23 under non-crosswind conditions. With the increase in the nose tip distance, C_p rapidly decreased to the minimum value of -0.19 and then increased sharply and stabilized. The pressure on the windward side near the tunnel exit decreased sharply. With the increase in the distance to the tunnel exit, the C_p value on the train windward side in the tunnel continued to decrease and then increased dramatically near the tail nose.

The position of the maximum positive C_p was 2.1 m in front of the head carriage nose, and the value was 0.33, after which it decreased rapidly to a stable value of about 0.1 when the train exited the tunnel under crosswinds. The C_p on the windward side varied suddenly, and the variation amplitude was considerably higher than that of non-crosswind conditions at the tunnel exit. The crosswind had little effect on the C_p of the train windward side in the tunnel. Therefore, the crosswind had a significant impact on the pressure on the windward side outside the tunnel, and the variation amplitude of C_p was much larger than that of the non-crosswind conditions.

The curves of C_p on the train leeward side are shown in Fig. 16(b). The C_p on the leeward side of the head carriage changed drastically. With the increase in the distance to the nose tip, the C_p on the leeward side decreased sharply first and then increased rapidly. The C_p on the
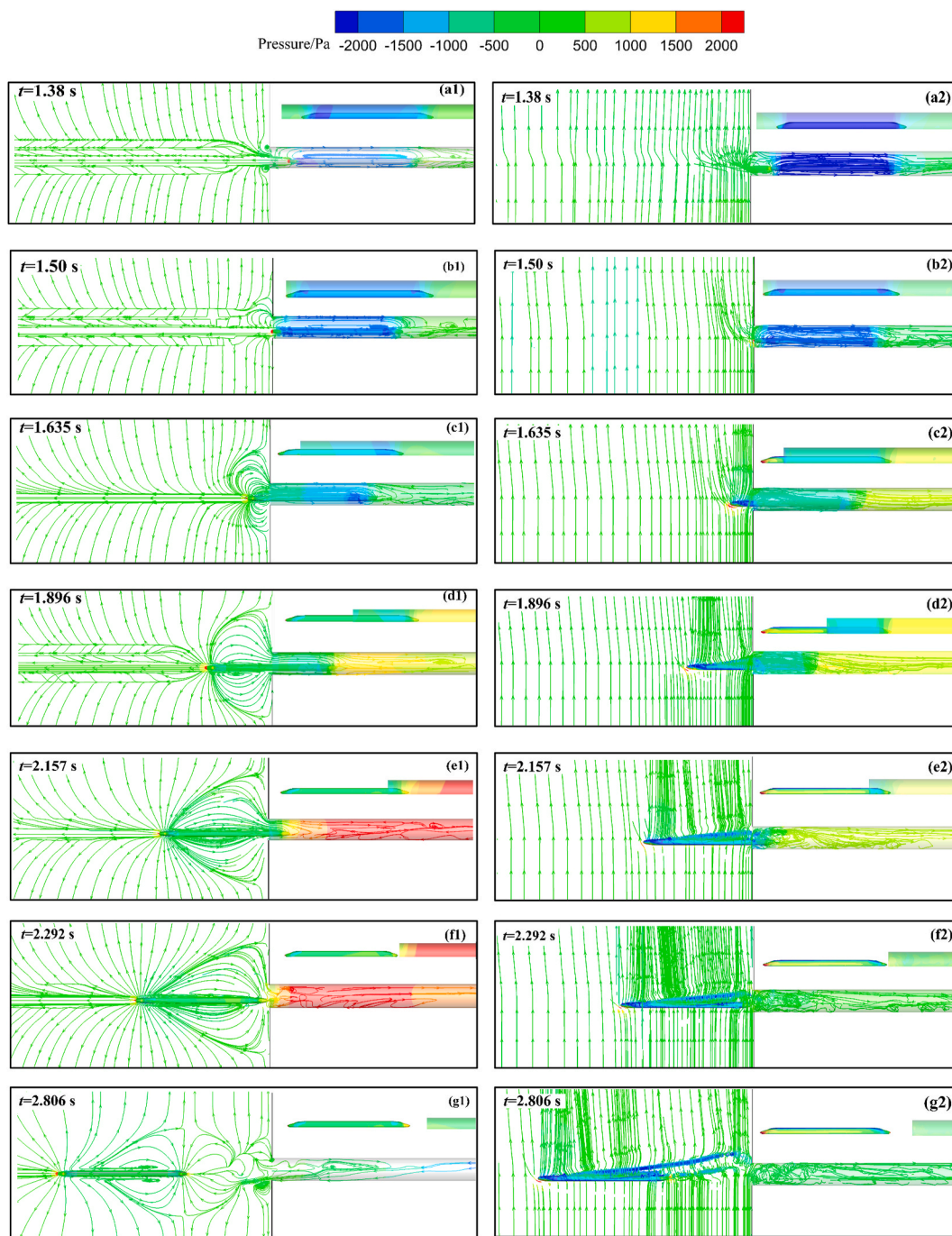
Fig. 11. Comparisons of 3D flow field when the train exited the tunnel under 0 m/s (left) and 30 m/s (right) crosswinds. $t = 1.38$ s: the distance between the nose tip of the head vehicle and the tunnel exit was about half the length of head vehicle; $t = 1.50$ s and 2.292 s: the nose tip of the head and rear vehicle arrived at the tunnel exit; $t = 1.635$ s, 1.896 s and 2.157 s: the middle of the head, middle and rear vehicle reached the tunnel exit; $t = 2.806$ s: the train exited the tunnel for 50 m.

leeward side of the middle carriage changed smoothly without crosswinds, while it showed significant fluctuations under crosswind conditions.

Fig. 17 shows Cp curves of the train top and bottom on the cross-sections through the train's axis. Cp variations at the top and bottom were the same with or without crosswinds. As the distance from the nose tip increased, the difference between the Cp at the top and bottom decreased gradually in both cases. The pressure at the top and bottom of the train fluctuated significantly under crosswind conditions. The pressure difference between the top and bottom of the train was small in the tunnel. The impact of the crosswind on the pressure on the top and bottom of the head vehicle was the most significant.

The peaks of the pressure coefficient on the train surface when the middle of the HST exited tunnel are summarized in Table 1. Under crosswind conditions, the peak positive and negative Cp values on the windward side of the train were 0.33 and −0.25, respectively, while the corresponding values with no crosswinds were 0.23 and −0.19. The ratios of the peak positive and negative Cp values were 1.44 and 1.32, respectively. The ratios of the peak positive Cp on the leeward, top, and bottom sides of the train under crosswinds were 0.17, 0.83, and 0.83, respectively, and the corresponding ratios of the peak negative Cp were 2.53, 3.50, and 3.57. Thus, it was concluded that under the influence of crosswinds, the pressure on the windward side and the negative pressure on the leeward side increased, while the positive pressure on the leeward
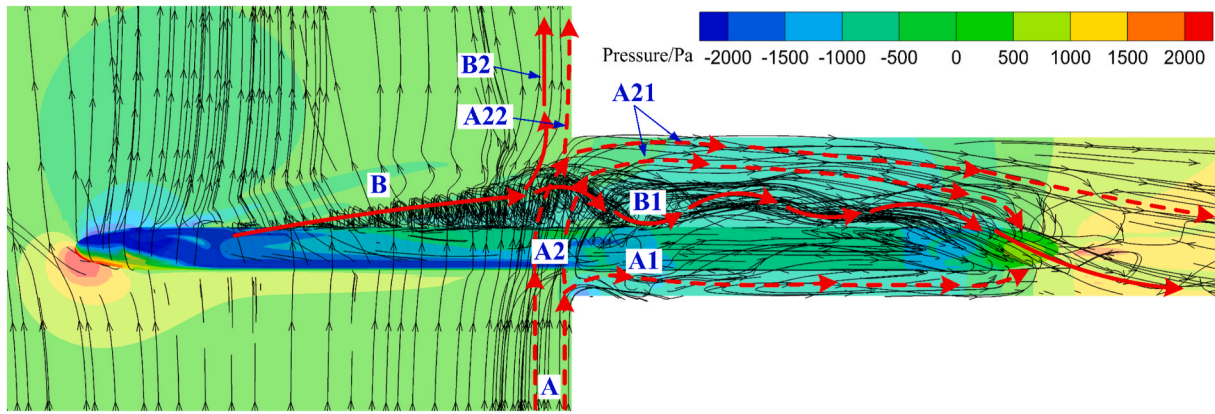
Fig. 12. Evolution of the flow field when the middle of the train arrived at the tunnel exit.
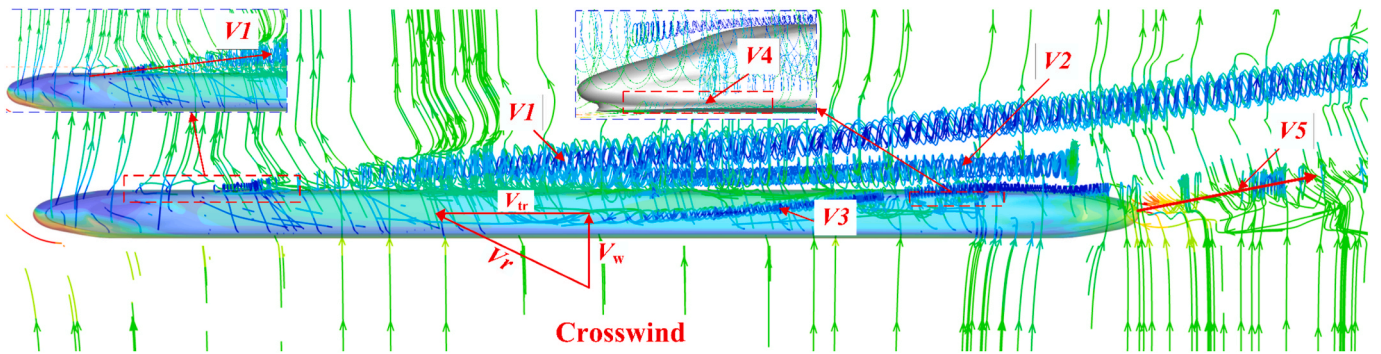

Fig. 13. Three-dimensional flow field around train when the tail nose exited the tunnel at 50 m.
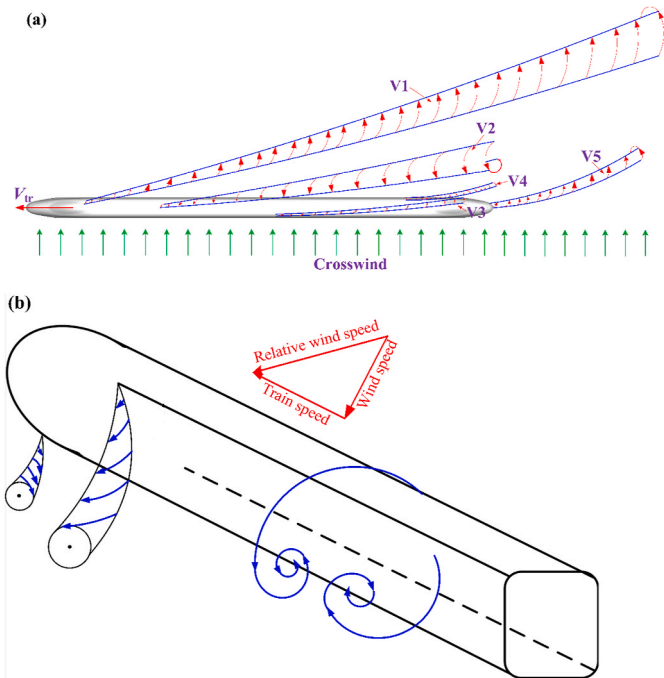

Fig. 14. Three-dimensional flow field: (a) simulation; (b) experiment by Chiu and Squire (1992).

side decreased. The positive pressure at the top and bottom of the train decreased, while the negative pressure increased.

4.3. Aerodynamic load

The aerodynamic load variations induced by the pressure change on the train surface significantly affect the safety of train operation. Fig. 18 shows the aerodynamic load curves as the train exited the tunnel, including the side force, lift force, and overturning moment. The left and right panels present the aerodynamic forces under non-crosswind and crosswind conditions, respectively.

The values of C_{side} of the head and rear carriages were very close, and the value of C_{side} of the middle carriage was close to 0 as the train moved through the tunnel without crosswinds. When the train exited the tunnel, the values of C_{side} of each carriage fluctuated significantly, and the variation amplitudes of the head, middle, and tail vehicles were 0.18, 0.01, and 0.52, respectively. The fluctuation amplitude of the tail carriage was the largest, followed by the head carriage, and that of the middle carriage was the smallest. This indicated that the swinging movement of the tail carriage was the most severe. After the train exited the tunnel completely, the values of C_{side} of each vehicle gradually tended to 0, as shown in Fig. 18 (a1).

When the train ran in the tunnel with crosswinds at the exit, the C_{side} value of each vehicle was the same as that of the train without crosswinds. When the train arrived at the tunnel exit, the C_{side} value of each carriage changed significantly. After the train left the tunnel, C_{side} gradually stabilized. The values of C_{side} of the head, middle, and trail carriage were 4.97, 1.85, and 0.62, respectively, and the corresponding variation amplitudes were 5.07, 2.03, and 1.86. The variation amplitude of the head carriage was the largest, and that of the tail vehicle was the smallest. The variation amplitudes of the head carriage under crosswind conditions were 28.2, 203, and 3.6 times those with non-crosswind
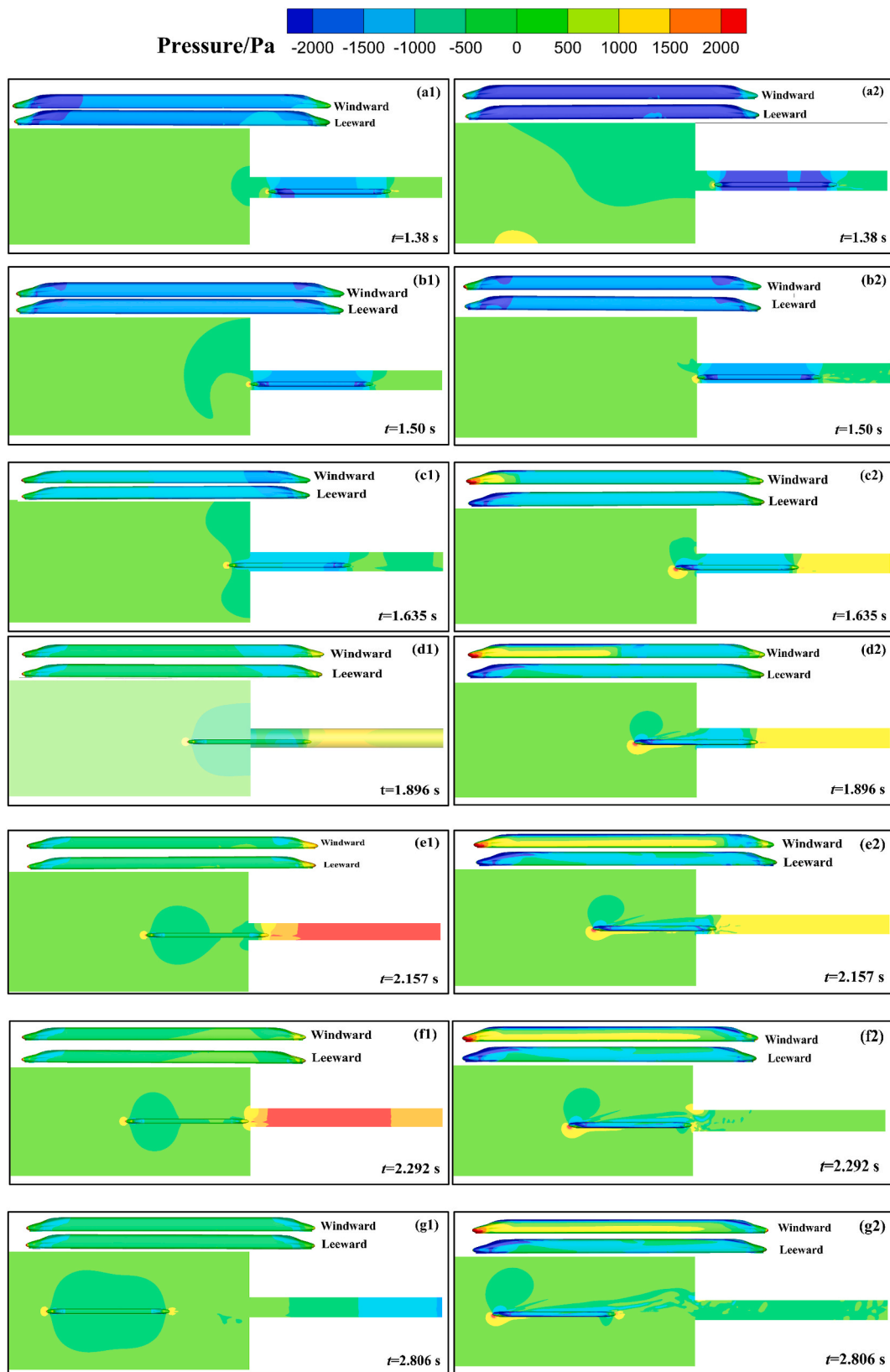
Fig. 15. Comparison of pressure field when train exited the tunnel under 0 m/s (left) and 30 m/s (right) crosswinds.

conditions, respectively. It should be noted that the variation of C_{side} was related to the position of the train marshalling. The side force decreased rapidly and then increased sharply as the train exited the tunnel, indicating that the train underwent swinging movement, shifting to the windward side first and then back to the leeward side. Furthermore, the swinging movement of the head carriage was more violent. The side force of the tail carriage increased dramatically and then decreased rapidly, indicating that the rear carriage underwent a lateral swinging
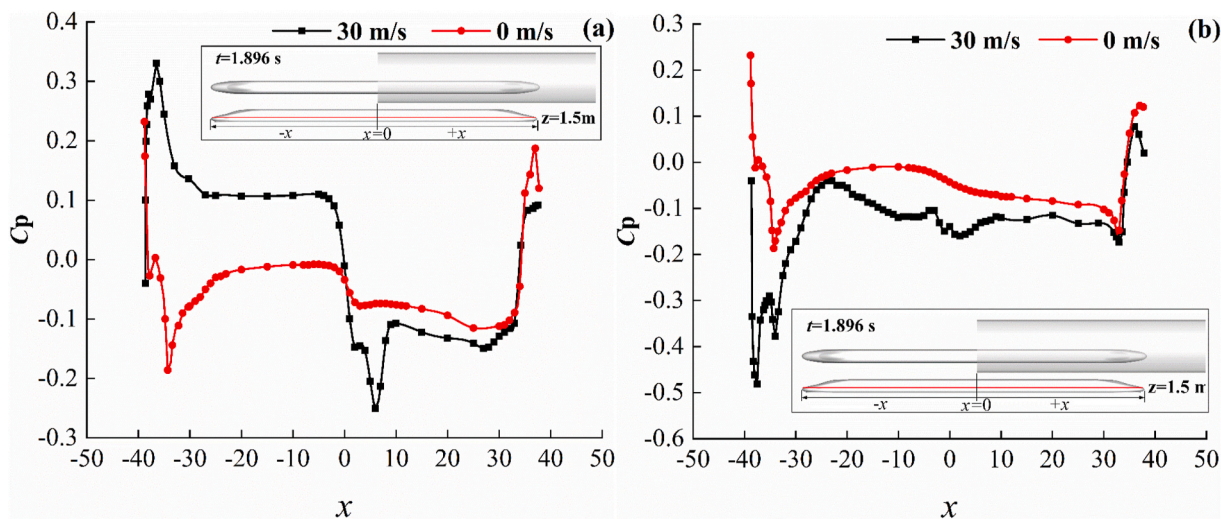
Fig. 16. Pressure coefficients on windward (a) and leeward (b) sides of train at height z = 1.5 m from the rail top when the middle of the train exited the tunnel.
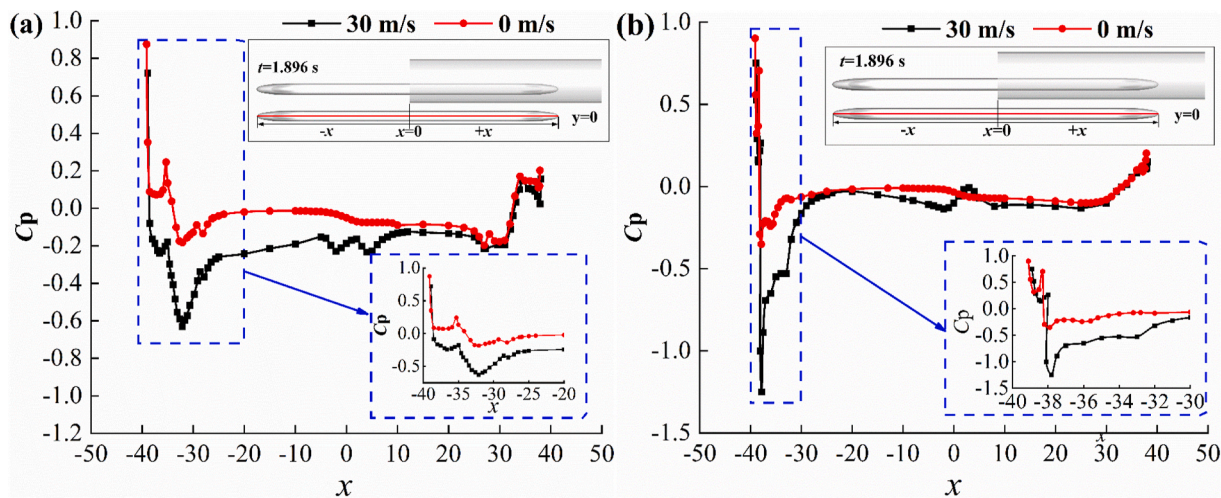

Fig. 17. Pressure coefficients on top (a) and bottom (b) of train at plane y = 0 when the middle of the train exited the tunnel.

Table 1
Pressure coefficient peak with tunnel exit under 0 m/s and 30 m/s crosswinds.

Position		Item	30 m/s	0 m/s	Peak to peak
z = 1.5 m	Windward	Maximum	0.33	0.23	1.44
		Minimum	−0.25	−0.19	1.32
	Leeward	Maximum	−0.04	0.23	0.17
		Minimum	−0.48	−0.19	2.53
y = 0 m	Top	Maximum	0.72	0.87	0.83
		Minimum	−0.63	−0.18	3.50
	Bottom	Maximum	0.75	0.90	0.83
		Minimum	−1.25	−0.35	3.57

motion that first moved to the leeward side and then shifted to the windward side. The side force gradually stabilized with small fluctuations after the train left completely, as shown in Fig. 18(a2). The overturning moments were calculated by computing the moment of the side force acting on the train center. Therefore, the variation of the overturning moment was the same as that of the side force, as shown in Fig. 18(c1) and (c2).

The curves of C_{lift} under non-crosswind conditions are shown in Fig. 18(b1). The variation amplitudes of C_{lift} of the head, middle, and rear vehicles were 0.36, 0.02, and 0.34, respectively. Thus, the variation amplitude of the head carriage was the largest, and that of the middle

carriage was the smallest. The C_{lift} value of the head vehicle decreased sharply when the head vehicle exited the tunnel. The C_{lift} value of the head vehicle was negative, and the direction was vertically downward after it exited the tunnel completely. The C_{lift} value of the middle carriage was maintained at about 0.07 during the exiting process, and the direction was upward. The value of C_{lift} of the rear vehicle was close to zero as it ran in the tunnel. When the tail carriage exited, the aerodynamic lift force experienced a sharp decrease and a rapid increase. After the tail carriage exited the tunnel fully, the aerodynamic lift gradually decreased to zero. The tail carriage exhibited vertical vibrations during the process of exiting the tunnel.

The values of C_{lift} of the vehicles fluctuated significantly when they exited the tunnel under crosswind conditions. After the train exited the tunnel, the lift forces of the head, middle, and trail carriages gradually stabilized, with values of −1.29, 0.67, and 0.40, respectively. The variation amplitudes of C_{lift} of the head, middle, and tail carriages were 1.23, 0.95, and 1.47, respectively. The aerodynamic lift of the tail carriage exhibited the largest variations, followed by the head carriage and the middle carriage. As the train exited the tunnel, each carriage vibrated vertically. After the tail carriage exited the tunnel, it experienced a regular vertical vibration.

It was concluded from the analysis above that the aerodynamic performance of a train deteriorates significantly when the train exits a
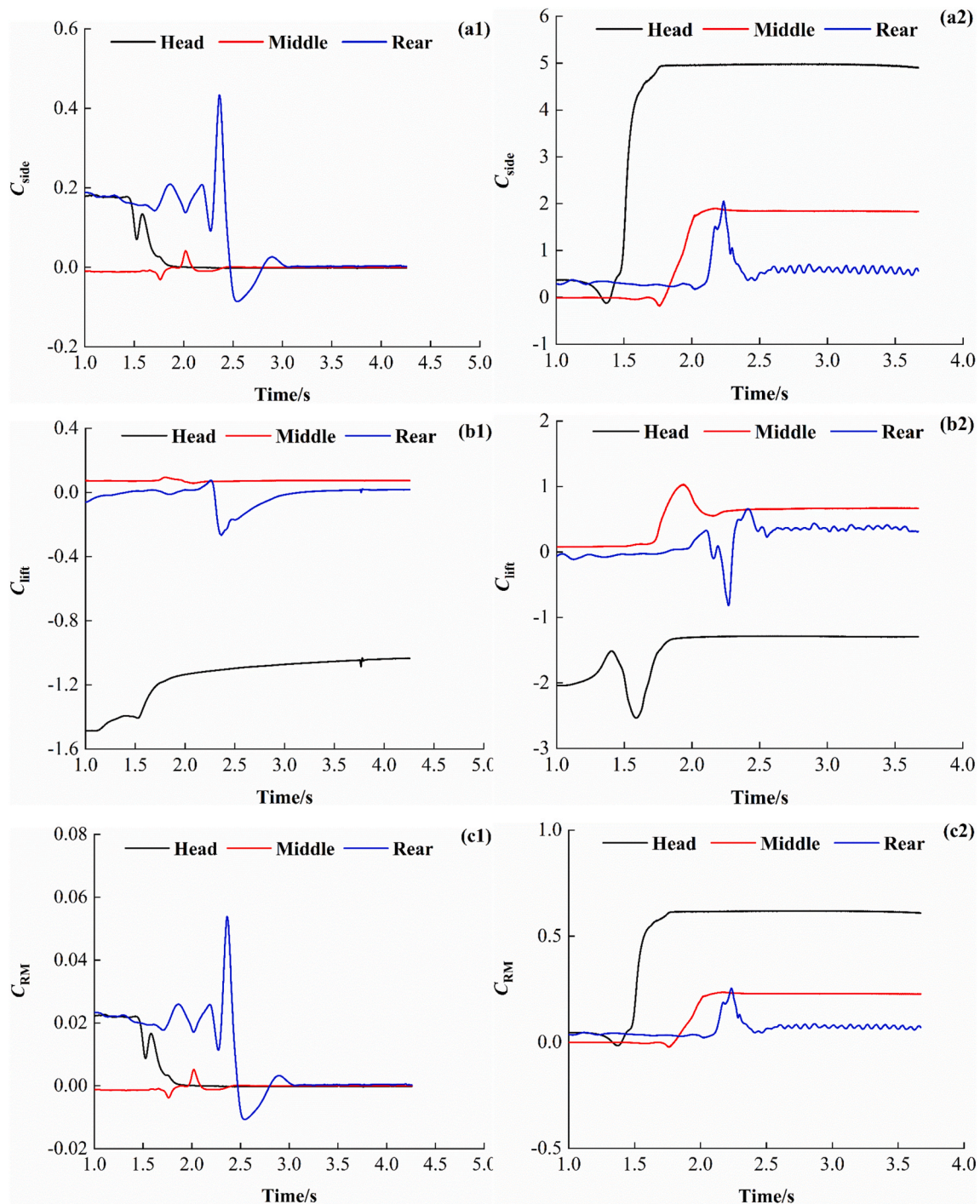
Fig. 18. Evolution of aerodynamic forces when train exited a tunnel with 0 m/s (left) and 30 m/s (right) crosswinds.

tunnel into crosswind conditions. The variation amplitudes of C_{side}, C_{lift}, and C_{RM} of the head carriage were the largest. Therefore, maintaining safety of the head carriage is the key to ensuring the safety of the entire train as it exits the tunnel under crosswind conditions.

5. Conclusions

Three-dimensional, compressible, and unsteady RANS method was adopted to investigate the aerodynamic loads and flow structures when a HST exited the tunnel and enter into a crosswind environment. The turbulent flow structures around the train were calculated by the SST $k - \omega$ turbulence model. The sliding mesh method was utilized to

implement the train movement relative to level ground. The numerical model was verified by comparison with the results from existing simulations and moving model tests. Based on this, we established the following conclusions:

(a) The flow structures and pressure field were symmetric as the HST exited the tunnel with non-crosswind. In contrast, the flow structure and pressure field distribution shown significant asymmetry in the horizontal plane as the train exited the tunnel under crosswinds.

(b) Under crosswind conditions, the flow structures varied transiently, which caused a sudden change in the pressure distribution on the train surface.

(c) The influence of the crosswinds on the surface pressure on the train windward and leeward surfaces was greater than that of the crosswinds on the aerodynamic pressure on the train bottom and top surfaces.

(d) The pressure on the train surface outside the tunnel was much more affected by crosswinds than the train inside the tunnel. The aerodynamic pressure on the train surface changed suddenly at the tunnel exit under crosswinds, especially the surface pressure of the head carriage.

(e) As the train exited the tunnel and enter into open air under crosswind conditions, the aerodynamic performance of the head carriage was the worst and the risk of accidents was the highest. Therefore, controlling the safety of the head vehicle is essential to ensuring the safety of the entire vehicle as it exits a tunnel into crosswind conditions.

Role of the funding source

CRediT authorship contribution statement

Lei Wang: Conceptualization, Methodology, Investigation, Data curation, Writing – original draft. **Jianjun Luo:** Conceptualization, Methodology, Resources, Supervision. **Feilong Li:** Software, Visualization, Data curation. **Dilong Guo:** Resources, Validation. **Liping Gao:** Writing – review & editing, Supervision. **Dengke Wang:** Writing – review & editing, Supervision.

Declaration of competing interest

The authors declare that they have no known competing financial interests or personal relationships that could have appeared to influence the work reported in this paper.

Acknowledgments

References

Baker, C., 2009. Cross-wind effects on road and rail vehicles. Veh. Syst. Dyn. 47 (8), 983–1022.

Baker, C.J., 2010. The simulation of unsteady aerodynamic cross wind forces on trains. J. Wind Eng. Ind. Aerod. 98, 88–99.

Baker, C.J., 1985. The determination of topographical exposure factors for railway embankments. J. Wind Eng. Ind. Aerod. 21, 89–99.

Baker, C.J., 2004. Measurements of the cross wind forces on trains. J. Wind Eng. Ind. Aerod. 92 (7–8), 547–563.

Baker, C.J., 1986. Train aerodynamic forces and moments from moving model experiments. J. Wind Eng. Ind. Aerod. 24, 227–251.

Baron, A., Mossi, M., Sibilla, S., 2001. The alleviation of the aerodynamic drag and wave effects of high-speed trains in very long tunnels. J. Wind Eng. Ind. Aerod. 89, 365–401.

Bocciolone, M., Cheli, F., Corradi, R., Muggiasca, S., Tomasini, G., 2008. Crosswind action on rail vehicles: wind tunnel experimental analyses. J. Wind Eng. Ind. Aerod. 96, 584–610.

BS EN 14067-6, 2018. Railway Applications–Aerodynamics Part 6: Requirements and Test Procedures for Cross Wind Assessment.

Catalano, P., Amato, M., 2003. An evaluation of RANS turbulence modelling for aerodynamic applications. Aerosp. Sci. Technol. 7, 493–509.

Cheli, F., Corradi, R., Rocchi, D., Tomasini, G., Maestrini, E., 2010. Wind tunnel tests on train scale models to investigate the effect of infrastructure scenario. J. Wind Eng. Ind. Aerod. 98, 353–362.

Chen, Z., Liu, T., Yu, M., Chen, G., Chen, M., Guo, Z., 2020. Experimental and numerical research on wind characteristics affected by actual mountain ridges and windbreaks: a case study of the Lanzhou-Xinjiang high-speed railway. Eng. Appl. Comp. Fluid 14, 1385–1403.

Chen, Z., Liu, T., Zhou, X., Niu, J., 2017. Impact of ambient wind on aerodynamic performance when two trains intersect inside a tunnel. J. Wind Eng. Ind. Aerod. 169, 139–155.

Chiu, T.W., Squire, L.C., 1992. An experimental study of the flow over a train in a crosswind at large yaw angles up to 90°. J. Wind Eng. Ind. Aerod. 45, 47–74.

Chu, C., Chien, S., Wang, C., Wu, T., 2014. Numerical simulation of two trains intersecting in a tunnel. Tunn. Undergr. Sp. Tech. 42 (5), 161–174.

Cooper, R.K., 1980. The Probability of Trains Overturning in High Winds. Wind Engineering, Pergamon, pp. 1185–1194.

Cooper, R.K., 1981. The effect of cross-winds on trains. J. Fluid. Eng.-T. ASME. 103 (1), 170–178.

Copley, J.M., 1987. The three-dimensional flow around railway trains. J. Wind Eng. Ind. Aerod. 26 (1), 21–52.

Deng, E., Yang, W., Lei, M., Zhu, Z., Zhang, P., 2019. Aerodynamic loads and traffic safety of high-speed trains when passing through two windproof facilities under crosswind: a comparative study. Eng. Struct. 188, 320–339.

Diedrichs, B., Sima, M., Orellano, A., Tengstrand, H., 2007. Crosswind stability of a high-speed train on a high embankment. P I Mech Eng F-J Rai. 221, 205–225.

Dorigatti, F., Sterling, M., Baker, C.J., Quinn, A.D., 2015. Crosswind effects on the stability of a model passenger train — a comparison of static and moving experiments. J. Wind Eng. Ind. Aerod. 138, 36–51.

Ferziger, J., Peric, M., 2002. Computational Method for Fluid Dynamics, third ed. Springer.

Ford, S.E., Riskowski, G., 2003. Effect of windbreak wall location on ventilation fan performance. Appl. Eng. Agric. 19, 343–346.

Fujii, T., Maeda, T., Ishida, H., Imai, T., Tanemoto, K., Suzuki, M., 1999. Wind-induced accidents of train/vehicles and their measures in Japan. Quarterly Report of RTRI 40, 50–55.

Gallagher, M., Morden, J., Baker, C., Soper, D., Quinn, A., Hemida, H., Sterling, M., 2018. Trains in crosswind – comparison of full-scale on-train measurements, physical model tests and CFD calculations. J. Wind Eng. Ind. Aerod. 175, 428–444.

Guo, Z., Liu, T., Chen, Z., Liu, Z., Monzer, A., Sheridan, J., 2020. Study of the flow around railway embankment of different heights with and without trains. J. Wind Eng. Ind. Aerod. 202, 104203.

Guo, Z., Liu, T., Yu, M., Chen, Z., Li, W., Huo, X., Liu, H., 2019. Numerical study for the aerodynamic performance of double unit train under crosswind. J. Wind Eng. Ind. Aerod. 191, 203–214.

He, K., Gao, G., Wang, J., Fu, M., Miao, X., Zhang, J., 2018. Performance of a turbine driven by train-induced wind in a tunnel. Tunn. Undergr. Sp. Tech. 82, 416–427.

He, X.H., Zou, Y.F., Wang, H.F., Han, Y., Shi, K., 2014. Aerodynamic characteristics of a trailing rail vehicles on viaduct based on still wind tunnel experiments. J. Wind Eng. Ind. Aerod. 135, 22–33.

Hemida, H., Krajnovi, S., 2010. LES study of the influence of the nose shape and yaw angles on flow structures around trains. J. Wind Eng. Ind. Aerod. 98, 34–46.

Hemida, H., Krajnovic, S., Davidson, L., 2005. Large-eddy Simulation of the Flow Around a Simplified High Speed Train under the Influence of a Cross-Wind, p. 5354.

Hoppmann, U., Koenig, S., Tielkes, T., Matschke, G., 2002. A short-term strong wind prediction model for railway application: design and verification. J. Wind Eng. Ind. Aerod. 90, 1127–1134.

Horvat, M., Bruno, L., Khris, S., Raffaele, L., 2020. Aerodynamic shape optimization of barriers for windblown sand mitigation using CFD analysis. J. Wind Eng. Ind. Aerod. 197, 104058.

Hosoi, T., Tanifuji, K., 2011. Influence of cross wind on derailment of railway vehicle running on curved track at low speed. Transactions of the Japan Society of Mechanical Engineers Series C 77, 381–391.

Khayrullina, A., Blocken, B., Janssen, W., Straathof, J., 2015. CFD simulation of train aerodynamics: train-induced wind conditions at an underground railroad passenger platform. J. Wind Eng. Ind. Aerod. 139, 100–110.

Khier, W., Breuer, M., Durst, F., 2000. Flow structure around trains under side wind conditions: a numerical study. Comput. Fluids 29, 179–195.

Li, T., Qin, D., Zhang, J., 2019. Effect of RANS turbulence model on aerodynamic behavior of trains in crosswind. Chin J Mech Eng-En. 32, 155–166.

Li, X., Wang, M., Xiao, J., Zou, Q., Liu, D., 2018. Experimental study on aerodynamic characteristics of high-speed train on a truss bridge: a moving model test. J. Wind Eng. Ind. Aerod. 179, 26–38.

Liu, T., Chen, Z., Zhou, X., Zhang, J., 2018. A CFD analysis of the aerodynamics of a high-speed train passing through a windbreak transition under crosswind. Eng. Appl. Comp. Fluid. 12, 137–151.

Miao, X., He, K., Minelli, G., Zhang, J., Gao, G., Wei, H., He, M., Krajnovic, S., 2020. Aerodynamic performance of a high-speed train passing through three standard tunnel junctions under crosswind. Appl Sci-Basel. 10, 3664.

Menter, F.R., Kuntz, M., Langtry, R., 2003. Ten years of industrial experience with the SST turbulence model. Turbulence, heat and mass transfer 4, 625–632.

Montenegro, P.A., Heleno, R., Carvalho, H., Calçada, R., Baker, C.J., 2020. A comparative study on the running safety of trains subjected to crosswind simulated with different wind models. J. Wind Eng. Ind. Aerod. 207, 104398.

Niu, J., Zhou, D., Liu, T., Liang, X., 2017. Numerical simulation of aerodynamic performance of a couple multiple units high-speed train. Veh. Syst. Dyn. 55, 681–703.

Rocchi, D., Tomasini, G., Schito, P., Somaschini, C., 2018. Wind effects induced by high speed train pass-by in open air. J. Wind Eng. Ind. Aerod. 173, 279–288.

Schober, M., Weise, M., Orellano, A., Deeg, P., Wetzel, W., 2010. Wind tunnel investigation of an ICE 3 endcar on three standard ground scenarios. J. Wind Eng. Ind. Aerod. 98, 345–352.

Sun, Z., Dai, H., Gao, H., Li, T., Song, C., 2019a. Dynamic performance of high-speed train passing windbreak breach under unsteady crosswind. Veh. Syst. Dyn. 57 (3), 408–424.

Sun, Z., Dai, H., Hemida, H., Li, T., Huang, C., 2019b. Safety of high-speed train passing by windbreak breach with different sizes. Veh. Syst. Dyn. 58 (12), 1935–1952.

Suzuki, M., Hibino, Y., 2016. Field tests and wind tunnel tests on aerodynamic characteristics of train/vehicles under crosswind. Quarterly Report of RTRI 57, 55–60.

Suzuki, M., Tanemoto, K., Maeda, T., 2003. Aerodynamic characteristics of train/vehicles under cross winds. J. Wind Eng. Ind. Aerod. 91, 209–218.

Tian, H., 2010. Research progress in railway safety under strong wind condition in China. J. of Central South Univ. (Sci. & Tech.). 41 (6), 2435–2443 (in Chinese).

Tomasini, G., Giappino, S., Corradi, R., 2014. Experimental investigation of the effects of embankment scenario on railway vehicle aerodynamic coefficients. J. Wind Eng. Ind. Aerod. 131, 59–71.

Wang, M., Li, X., Xiao, J., Sha, H., Zou, Q., 2020. Effects of infrastructure on the aerodynamic performance of a high-speed train. P. I. Mech. Eng. F-J. Rai. 1791156491.

Xiang, H., Li, Y., Chen, S., Hou, G., 2018. Wind loads of moving vehicle on bridge with solid wind barrier. Eng. Struct. 156, 188–196.

Xiang, X.T., Xue, L.P., 2010. Tunnel hood effects on high speed train-tunnel compression wave. Journal of Hydrodynamics. Ser. Bull. 22 (5), 940–947.

Xue, F., Han, Y., Zou, Y., He, X., Chen, S., 2020. Effects of wind-barrier parameters on dynamic responses of wind-road vehicle–bridge system. J. Wind Eng. Ind. Aerod. 206, 104367.

Yang, Q., Song, J., Li, D., Zhang, J., Yang, G., 2013. Train model acceleration and deceleration. Sci China Technol Sc 56, 642–647.

Yang, Q., Song, J., Yang, G., 2016. A moving model rig with a scale ratio of 1/8 for high speed train aerodynamics. J. Wind Eng. Ind. Aerod. 152, 50–58.

Yang, W., Deng, E., Lei, M., Zhang, P., Yin, R., 2018. Flow structure and aerodynamic behavior evolution during train entering tunnel with entrance in crosswind. J. Wind Eng. Ind. Aerod. 175, 229–243.

Yang, W., Deng, E., Zhu, Z., Lei, M., Shi, C., He, H., 2020. Sudden variation effect of aerodynamic loads and safety analysis of running trains when entering tunnel under crosswind. Appl. Sci. 10, 1445.

Yao, Z., Zhang, N., Chen, X., Zhang, C., Xia, H., Li, X., 2020. The effect of moving train on the aerodynamic performances of train-bridge system with a crosswind. Eng. Appl. Comp. Fluid. 14, 222–235.

Zhang, J., Gao, G., Liu, T., Li, Z., 2015. Crosswind stability of high-speed trains in special cuts. J. Cent. South Univ. (Sci. & Tech.). 22, 2849–2856.

Zhou, X., Liu, T., Chen, Z., Zou, X., Liu, D., 2017. Effect of ambient wind on pressure wave generated by high-speed train entering a tunnel. J. Cent. South Univ. (Sci. & Tech.). 24, 1465–1475.

Zhuang, Y., Lu, X., 2015. Numerical investigation on the aerodynamics of a simplified high-speed train under crosswind. Theor. App. Mech. Lett. 5, 181–186.